
Article:
Mei, Z.T., Li, G.J. orcid.org/0000-0002-5956-4033, Zhu, Z.Q. orcid.org/0000-0001-7175-3307 et al. (3 more authors) (2023) Scaling effect on inter-turn short-circuit fault of PM machines for wind power application. IEEE Transactions on Industry Applications, 59 (1). pp. 789-800. ISSN 0093-9994

https://doi.org/10.1109/TIA.2022.3211249

Scaling Effect on Inter-Turn Short-Circuit Fault of PM Machines for Wind Power Application

Z. T. Mei[1], G. J. Li[1], *Senior Member*, *IEEE*, Z. Q. Zhu[1], *Fellow*, *IEEE*, R. Clark[2], A. Thomas[2] and Z. Azar[2]
[1]Department of Electronic and Electrical Engineering, The University of Sheffield, Sheffield, UK
[2]Siemens Gamesa Renewable Energy Limited, North Campus, Broad Lane, Sheffield, UK
g.li@sheffield.ac.uk

***Abstract*—This paper proposes a general analytical model of surface-mounted permanent magnet (SPM) machines with series-connected coils under inter-turn short circuit (ITSC) fault. One prominent feature of this fault model is that the air-gap and slot-leakage components of inductances under fault are calculated separately, and the influences of pole number and spatial distribution of coils have been considered in the calculations. In the model, the winding function approach (WFA) is used to calculate the air-gap inductance components by considering all space harmonics whilst slot-leakage inductance components are obtained by using slot permeance method. The proposed fault model built in Matlab/Simulink is validated by time stepping FE simulations for a 3kW 96-slot 32-pole SPM machine. The fault model has acceptable accuracy and is suitable for the fast evaluation of fault performance of SPM machines and its accuracy considering core saturation can be improved using FE-based results. Other power ratings (0.5MW and 3MW) have also been investigated to study the scaling effect on machine fault-tolerant capability. A 12-slot 4-pole small scale prototype has been built to validate the developed fault models.**

***Index Terms*—inter-turn short-circuit, permanent magnet machine, scaling effect, slot permeance, winding function approach (WFA).**

I. Introduction

As wind power capacity in the global market is increasing rapidly, reducing the cost of energy becomes an important issue. It has been reported that the operation and maintenance costs accounted for 10% to 25% of the total income of a wind farm [1], [2]. Therefore, fault diagnosis of wind turbines is important to reduce the operation and maintenance costs in order to make wind energy more economical. Compared with faults in other major components of wind turbines, the downtime of wind generators was the longest, up to 7 days, in which winding faults accounted for 20% of the overall faults [3], [4]. There are five major types of winding faults for wind generators, whether they are doubly-fed induction generators (DFIG) or promising permanent magnet generators, namely (1) inter-turn (turn-to-turn) short circuit (ITSC), (2) coil to coil short circuit, (3) open circuit of one phase, (4) phase to phase short circuit, and (5) coil/phase to ground short circuit [5]. Amongst all these faults, the ITSC fault was perceived to be the early stage of other more severe faults. Due to the above reasons, it is important to detect and mitigate such faults before they escalate. Regarding fault detection and mitigation, physics-based fault modelling is often regarded as a good starting point to propose effective model-based methods.

For physics-based modelling of permanent magnet (PM) machines under ITSC fault, there are three major methods in literature: (1) winding function approach (WFA) [6]–[10], (2) finite element (FE) approach [11]–[13], and (3) magnetic equivalent circuit (MEC) approach [14], [15]. WFA is a circuit-based modelling method in essence, and it is the foundation of analytical derivation and calculation of inductances of integer-slot AC machines [16]. Researchers in [6], [17] have tried to use this method to analyze the fault performance of induction and synchronous machines in the last 30 years. The disadvantage of this method for calculating the inductances is that it neglects the core saturation and also space harmonics. If space harmonics are considered, the derivation of general inductance expressions under faulty conditions for machines with complex winding configurations will become significantly difficult. Considering this difficulty in employing the WFA, researchers in [18]–[20] made assumptions to simplify the determination of the fault inductances in the fault model based on the relationship between the healthy inductances and the number of turns. However, when large number of coils per phase are located in different slots around the stator periphery, such assumptions may not be valid. Unlike WFA, both FE and MEC approaches can consider the core saturation. However, they require detailed geometrical dimensions of the machines, and simulations using these two methods are much more time-consuming. Using the FE model as an example, a total computation time of several days or even months if sinusoidal voltage source and full model are employed for large direct-drive wind power generators with large numbers of stator slots and rotor poles.

Therefore, WFA will be adopted for the analyses of integer-slot SPM machines with a slot/pole/phase (SPP) of 1 in this paper. However, it was found that the simulated results using the air-gap inductance components calculated by WFA with all space harmonics considered cannot match well with that of 2D FE simulations even when linear magnetic material was used. This is due to the fact that for surface-mounted PM (SPM) machines, the slot-leakage inductance components will also have some influence on machine performance due to large effective air gaps. To establish a more accurate analytical fault model, the slot-leakage inductances will be calculated based on the slot permeance method and are added to the corresponding air-gap inductance components. The proposed fault model built in Matlab/Simulink is validated by time stepping FE simulations. In addition, a comparison between the developed model in this paper against the analytical model proposed in

[18] has been carried out. The comparative results show that the influence of pole number and spatial distribution of coils on determination of inductance values under faulty conditions cannot be neglected when the number of short-circuited turns in one coil is large. Furthermore, the proposed analytical model could be used to reduce the number of FE simulations to develop a more accurate fault model considering core saturation if necessary. The SPM machines with different power-ratings, e.g. 3kW, 0.5MW and 3MW will also be investigated to analyse the effect of scaling on the ITSC fault performance by using the proposed model. To validate the developed fault models, a small scale 12-slot 4-pole SPM machine has been built and tested.

II. Modelling of ITSC Fault of SPM Wind Generator

A. Analytical Modelling Neglecting Saturation

An example of ITSC fault in a stator armature coil of wind power generator is shown in Fig. 1. Due to a turn insulation breakdown, two electrically isolated points will have an electrical contact, leading to an ITSC fault and a large short-circuit current, which can cause local overheating, speeding up the insulation breakdown of the entire armature windings.

The equivalent circuit of the ITSC fault in a wye-connected stator winding of a PM machine is shown in Fig. 2, where the fault is assumed to occur in phase A. The parameters shown in Fig. 2 will be explained in detail later. This equivalent circuit will be used to build the electrical model of the studied PM machines. Together with the mechanical model, tools like Matlab/Simulink can be used to investigate the influence of ITSC fault on PM machine's performance.

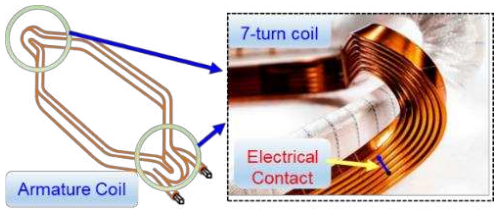

Fig. 1 ITSC fault in armature coils.

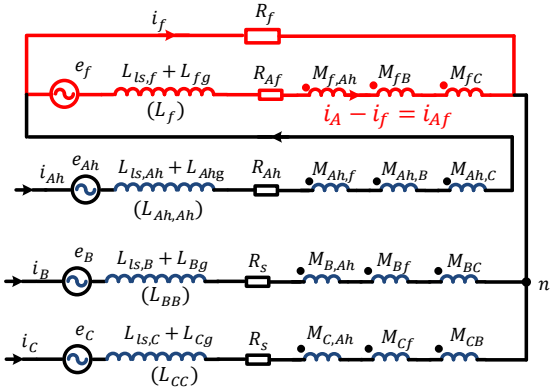

Fig. 2 Equivalent circuit of PM machines under ITSC fault in the phase A.

From Fig. 2, the circuit-based voltage equations representing the relationship between phase voltages, EMFs and also currents under ITSC fault can be expressed as (1), where R_s is the phase resistance, R_{Af} is the resistance of short-circuited turns, and R_f (assumed to be zero for the 3kW machine) is the contact resistance between short-circuited points. $M_{Ah,f}$, M_{Bf}, and M_{Cf} are the mutual inductances between the remaining healthy winding Ah, healthy windings B, C and short-circuited turns, respectively. L_f is the self-inductance of short-circuited turns. $i_{Ah}(=i_A)$, i_B and i_C are the currents of remaining healthy windings Ah, B and C, respectively. Similarly, e_A, e_B, and e_C are the phase back EMFs of healthy phase windings. In addition, $e_{Ah}=(1-\mu)e_A$, $e_f=\mu e_A$, in which the phase faulty turns ratio in one phase winding is defined as $\mu=\frac{1}{p}\mu_1=\frac{1}{p}\frac{n_f}{n_c}$ for the studied integer-slot SPMs with a SPP of 1. The corresponding coil faulty turns ratio in one elementary coil is defined as $\mu_1=n_f/n_c$, where n_f denotes the number of short-circuited turns in one coil, and n_c describes the number of turns per coil. Furthermore, p is the number of pole pairs.

$$\begin{bmatrix} v_A \\ v_B \\ v_C \\ 0 \end{bmatrix} = \begin{bmatrix} R_s & 0 & 0 & -R_{Af} \\ 0 & R_s & 0 & 0 \\ 0 & 0 & R_s & 0 \\ R_{Af} & 0 & 0 & -R_{Af}-R_f \end{bmatrix} \begin{bmatrix} i_A \\ i_B \\ i_C \\ i_f \end{bmatrix} + \begin{bmatrix} e_A \\ e_B \\ e_C \\ e_f \end{bmatrix} + \begin{bmatrix} L_{AA} & M_{AB} & M_{AC} & -(M_{Ah,f}+L_f) \\ M_{BA} & L_{BB} & M_{BC} & -M_{Bf} \\ M_{CA} & M_{CB} & L_{CC} & -M_{Cf} \\ (M_{f,Ah}+L_f) & M_{fB} & M_{fC} & -L_f \end{bmatrix} \frac{\mathrm{d}}{\mathrm{d}t} \begin{bmatrix} i_A \\ i_B \\ i_C \\ i_f \end{bmatrix} \tag{1}$$

If the phase back EMFs in (1) contain harmonics and no neutral line is introduced, then the phase voltages cannot be directly obtained from the line voltages under ITSC fault. This means that the sum of the 3 phase voltages will be

$$v_A+v_B+v_C=(e_A+e_B+e_C)-R_{Af}i_f - \left(L_f+M_{Ah,f}+M_{Bf}+M_{Cf}\right)\frac{\mathrm{d}i_f}{\mathrm{d}t} \tag{2}$$

Equation (2) together with (3) and (4) could be used to calculate the phase voltages from line voltages.

$$v_{AB}=v_A-v_B \tag{3}$$

$$v_{BC}=v_B-v_C=v_A+2v_B-(v_A+v_B+v_C) \tag{4}$$

Once the currents in the healthy and faulty windings are determined, the electromagnetic torque under ITSC fault can be calculated by

$$T_e=p\frac{\left(e_Ai_A+e_Bi_B+e_Ci_C-e_fi_f\right)}{\omega_r}+T_{cog} \tag{5}$$

where ω_r is the rotor electrical speed (rad/s), T_{cog} is the cogging torque.

The above equations will be used in the Matlab/Simulink to analytically predict the machine's performance before and after ITSC faults. It should be mentioned that the phase back EMFs and cogging torque obtained from FE simulations of healthy machines are imported into the Matlab/Simulink to accurately predict the torque ripple before and after introducing the ITSC fault. In addition, inductances in the fault model will be calculated based on the analytical method (which needs the machine's geometrical dimensions) in the following sections.

B. Analytical Modelling Considering Saturation

If core saturation needs to be fully included into the analytical modeling based on Matlab/Simulink, its influence on apparent and differential inductances together with PM flux

linkages should be taken into account. In order to consider the saturation effect, in [21], the flux linkage lookup table based model is used. However, such a model does not provide meaningful physical insights into the fault phenomena and multiple fault scenarios might not be easily incorporated. Furthermore, there is no detailed discussion about how to determine the current profiles as inputs to obtain the stator flux linkages. In [22], lookup tables using differential inductances considering core saturation are employed. However, only the influence of core saturation on differential/incremental inductances is considered, and the influence of core saturation on on-load PM flux linkages and apparent inductances has not been included because the frozen permeability method such as investigated in [23], [24] has not been employed. In order to overcome the shortcomings in existing methods, the frozen permeability method has been used in this paper to obtain saturated apparent inductances and on-load PM flux linkages of the studied machines under different operating conditions.

In the frozen permeability method, accurate determination of the current profiles as inputs to obtain the permeability in every mesh element in the FE model is the key to achieving the saturated apparent inductance and on-load PM flux linkage look-up tables. For 3-phase healthy machines, the currents are often balanced and their waveforms are sinusoidal. However, this is no longer the case for faulty machines, especially when significant harmonics exist in their phase back EMFs. A proposed method making full use of the linear analytical model (based on Matlab/Simulink) developed in this paper is shown in Fig. 3. As illustrated in Fig. 3, the current profiles as inputs into non-linear FE fault models could be determined by the linear analytical model. This can help to update the saturated apparent inductance and on-load PM flux-linkage under different operating conditions. If necessary, this method can be iterated to further improve the model's accuracy. Meanwhile, a predefined current accuracy of 5% (deemed acceptable for most cases) or a maximum number of iterations of 5 can be selected to terminate the iteration, which are similar to the settings in the FE modelling (JMAG software package).

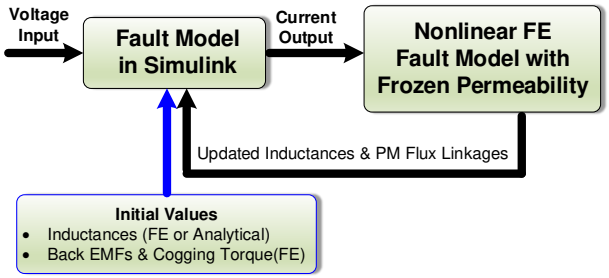

Fig. 3 Analytical modelling (based on Matlab/Simulink) of ITSC fault with consideration of core saturation.

C. FE Numerical Modelling

To validate the results obtained by the developed analytical models, 2D FE simulations (JMAG software package) for the outer rotor 3kW 96-slot/32-pole SPM machine have been carried out in this paper. Since the machines under ITSC fault become asymmetric, a full FE model is necessary as shown in Fig. 4, where only part of the model is shown to have a clearer view of the ITSC fault. Furthermore, the faulty machine is excited by voltage sources to fully reflect the fault characteristics in FE simulations, as shown in Fig. 5. In Fig. 4, the 15 healthy coils are represented by one FEM coil (A_1_15) in the FE simulation and the faulty coil with the ITSC fault is represented by three FEM coils in Fig. 5. For example, the remaining healthy turns at the bottom, the top, and the short-circuited turns in the middle of the affected slot are represented by A_16_hb, A_16_ht, and A_16_fm, respectively. This arrangement will lead to balanced three phase back EMFs when the switch in Fig. 5 is off, i.e., the machine is healthy.

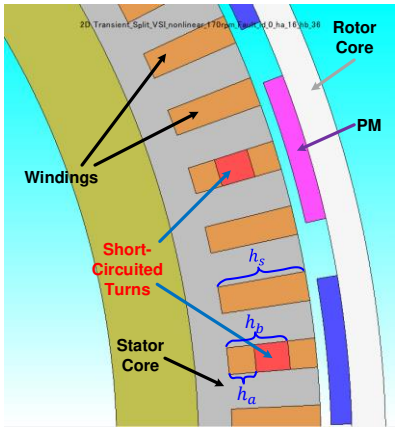

Fig. 4 Cross-sectional view of the machines with the ITSC fault for FE simulations.

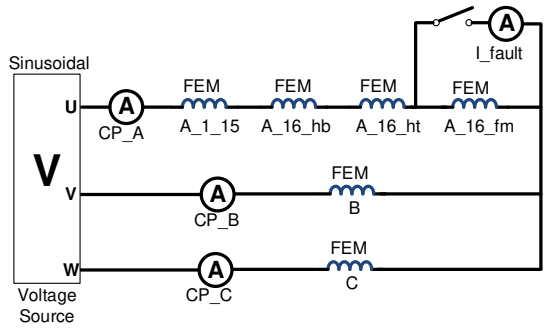

Fig. 5 External circuit for the ITSC fault simulations.

III. Inductance Calculation

One of the most important parts of fault modeling is to determine the model's parameters, especially the inductances. Experimental measurement and theoretical calculation are two typical ways to obtain inductances of a machine's model. However, experimental measurement of inductances for different fault scenarios (under ITSC faults) would be inconvenient, and even impossible at a machine design stage. In [18]–[20], the researchers have made a simple assumption about the determination of the elements in the faulty inductance matrix (under ITSC fault), which assumes that they could be obtained by calculating the inductances of the healthy machines. However, the validity of that assumption under fault are neither confirmed by FE simulations nor by the conventional inductance calculation method, i.e., WFA. Hence, whether it could be applied to multipole SPM machines is questionable. The only advantage of making that simple assumption is that a faulty inductance matrix could be determined from the calculated or measured phase self- and mutual-inductances of the healthy machines. In [25], a more accurate approach, based on FE modelling only, is adopted to calculate the inductances under ITSC fault. One important

conclusion in [25] is that the pole number has a significant influence on the values of the inductance of the short-circuited turns under ITSC fault. However, the assumption that the mutual-inductances between any two coils are the same is not valid, which can be proven by the WFA and FE. This is mainly because coils that are closer to each other will have larger mutual-inductances, whilst the ones that are further apart will have smaller mutual-inductances.

A. *Calculation of Inductances*

In [26], the phase self- and mutual-inductances are considered to have three components:

$$\begin{cases} L_{ph} = L_g + L_{ls} = L_g + L_{slot} + L_{end} \\ M_{ph} = M_g + M_{ls} = M_g + M_{slot} + M_{end} \end{cases} \tag{6}$$

where L_g, M_g are the air-gap components and L_{ls}, M_{ls} are the leakage components, respectively. L_{slot} , M_{slot} are the slot-leakage components, and L_{end} and M_{end} are the end-turn leakage components, respectively. It is worth noting that for long-drum-type SPM machines, the end-winding leakage components can be neglected. Therefore, 2D FE simulation is enough to ensure the accuracy of the calculated inductances.

The final inductance matrix now is split into two parts, i.e., air-gap component $\boldsymbol{L}'_{ms}$ and slot-leakage component $\boldsymbol{L}'_{ls}$.

$$\begin{bmatrix} L_{AA} & M_{AB} & M_{AC} & -(M_{f,Ah} + L_f) \\ M_{BA} & L_{BB} & M_{BC} & -M_{Bf} \\ M_{CA} & M_{CB} & L_{CC} & -M_{Cf} \\ (M_{f,Ah} + L_f) & M_{fB} & M_{fC} & -L_f \end{bmatrix} = \boldsymbol{L}'_{ms} + \boldsymbol{L}'_{ls} \tag{7}$$

Calculation of air-gap inductance components is done by WFA. Air-gap component of inductances can be calculated by [27]:

$$L_{ij} = \frac{\mu_0 r_e l_{stk}}{g_e} \int_0^{2\pi} N_i(\phi_s) N_j(\phi_s)\, d\phi_s \tag{8}$$

where l_{stk} is the effective stack length, r_e is the mean air-gap radius, g_e is the effective air-gap length, μ_0 is the permeability of free space. Both g_e and r_e for SPM machines can be calculated using the method in [26]. $N_i(\phi_s)$ and $N_j(\phi_s)$ are the winding functions of the ith and jth windings, respectively. When an ITSC fault happens, the healthy phase winding is split into two parts: faulty winding and remaining healthy winding. The corresponding winding functions after fault (the influence of the slot opening on the derivation of winding functions is neglected) is illustrated in Fig. 6, which will be used to get the air-gap components of the inductances in these two windings.

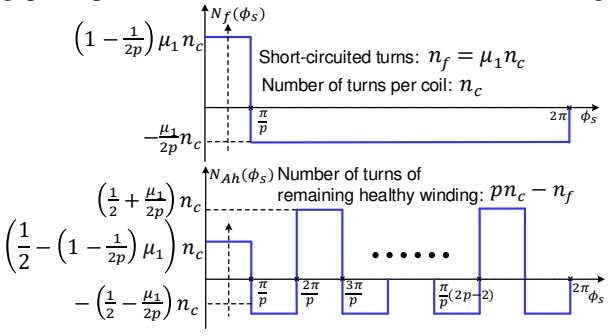

Fig. 6 Winding functions of faulty winding (Phase A).

The air-gap inductance component of phase A is

$$L_{Ag} = \frac{\mu_0 r_e l_{stk}}{g_e} \frac{\pi}{2} (n_c)^2 \tag{9}$$

After some arrangements, the air-gap component inductance matrix is expressed as follows:

$$\boldsymbol{L}'_{ms} = L_{Ag} \begin{bmatrix} 1 & -\frac{1}{3} & -\frac{1}{3} & -\mu \\ -\frac{1}{3} & 1 & -\frac{1}{3} & \frac{\mu}{3} \\ -\frac{1}{3} & -\frac{1}{3} & 1 & \frac{\mu}{3} \\ \mu & -\frac{\mu}{3} & -\frac{\mu}{3} & -\mu^2(2p-1) \end{bmatrix} \tag{10}$$

Slot-leakage inductance component calculation is based on the slot permeance method in [28]. For the studied PM machines with open slot shown in Fig. 7, the slot-leakage inductance components can be written as

$$\boldsymbol{L}'_{ls} = \begin{bmatrix} L_{ls,A} & 0 & 0 & -(M_{ls\_Ah,f} + L_{ls,f}) \\ 0 & L_{ls,B} & 0 & 0 \\ 0 & 0 & L_{ls,C} & 0 \\ M_{ls\_Ah,f} + L_{ls,f} & 0 & 0 & L_{ls,f} \end{bmatrix} \tag{11}$$

where $L_{ls,A}$, $L_{ls,B}$, $L_{ls,C}$, $L_{ls,f}$ are the slot-leakage components of self-inductances of phases A, B and C and short-circuited turns, respectively. $M_{ls\_Ah,f}$ is the slot-leakage component of mutual inductance between the remaining healthy phase winding and short-circuited turns.

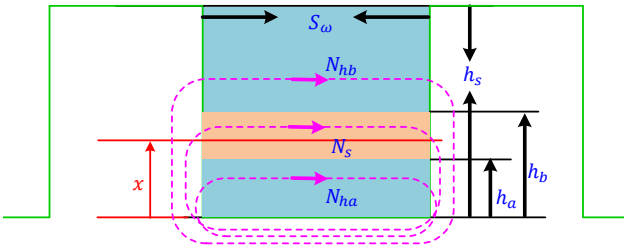

Fig. 7 Flux distribution in open slot caused by remaining healthy winding.

According to Fig. 7, the unknown inductances in the slot-leakage inductance matrix are derived as

$$L_{ls,A} = L_{ls,B} = L_{ls,C} = 2p\mu_0 l_{stk} \left(\frac{n_c}{h_s}\right)^2 \frac{(h_s)^3}{3S_\omega} \tag{12}$$

$$L_{ls,f} = 2\mu_0 l_{stk} \left(\frac{n_c}{h_s}\right)^2 \frac{(h_b - h_a)^2}{S_\omega} \left(h_s - \frac{1}{3}h_a - \frac{2}{3}h_b\right) \tag{13}$$

$$M_{ls\_f,Ah} = M_{ls\_Ah,f} = 2\mu_0 l_{stk} \left(\frac{n_c}{h_s}\right)^2 \left[\frac{h_a(h_b - h_a)^2}{2S_\omega} + \frac{(h_b - h_a)}{2S_\omega}\{(h_s - h_b + h_a)^2 - h_a^2\}\right] \tag{14}$$

where S_ω is the slot width, h_s is the slot height, h_a and h_b represent the fault locations along the slot, shown in Fig. 4, and $n_f = n_c(h_b - h_a)/h_s$ represents the number of short-circuited turns.

B. *Results of Inductances*

To simplify the inductance calculation by FE simulations, one coil short-circuit fault is assumed for 3kW, 0.5MW and 3MW SPM machines. The machine specifications are given in Table I, in which the rated voltage and current of the 0.5MW, 3MW are adjusted due to the change of series/parallel

connected coils into series connected coils. To be consistent with the WFA, in the FE model, permanent magnets have been replaced by air, and the stator and rotor cores are assumed to be linear magnetic material with a relative permeability $\mu_r = 10000$. The self- and mutual-inductances of the 3kW machine calculated by FE and analytical methods are shown in Table II. It can be found that there is generally a reasonably good match between the FE and analytical results although discrepancy for the mutual inductances is relatively larger. This relatively large difference in mutual inductances is mainly due to the fact that, in the WFA, the negative part of the air-gap flux density (or magneto-motive force) generated by the short-circuited coil is assumed to be constant at different angular positions, as shown in Fig. 6. This is not the case predicted by the FE model, which shows air-gap flux density far away from the short-circuited coil has reduced value. This is the same for the 0.5MW and 3MW SPM machines, but due to space limitations, their results have not been included in this paper.

Table I Key parameters of the studied SPM machines

Rated power	3kW	0.5MW	3MW
Rated speed (rpm)	170	32	15
Line-line rated voltage (Vrms)	690	4830	13800
Phase current (Arms)	2.5	62.6	139.5
Series turns/coil	52	23	14
Numbers of slots/poles	96/32	294/98	480/160
Rotor outer diameter (mm)	426.4	2195.5	5000
Stack length (mm)	110	550	1200
Airgap length (mm)	2	2.15	5

Table II Inductances in mH of the 3kW machine under one coil short-circuit fault

Inductance/Method	$L_{AA}/L_{BB}/L_{CC}$	$M_{BC}/M_{AC}/M_{AB}$	M_{Bf}/M_{Cf}	$M_{Ah,f}$
2D FE	31.62	-6.1	-0.382	-1.038
Analytical	31.96	-6.627	-0.414	-1.165
Error	1.1%	8.6%	8.4%	12.2%

IV. Simulation Results

A. One Coil Short-Circuit Fault

Due to the limitation of voltage source excitation in the FE simulations, three phase balanced sinusoidal voltages are fed to the studied 3kW SPM machine and its rotor mechanical speed is kept constant during the whole operating period. It is worth mentioning that FE simulations for the 0.5MW and 3MW SPM machines using the same method with the Dell Precision Tower 5820 PC workstation took more than one month to complete, hence the FE simulations for those machines using voltage source excitation have not been carried out. In this section, one coil short-circuit fault has been selected as an example, and the results for a single turn short-circuit will be introduced in section IV.B.

a. Linear Magnetic Core Material

To validate the proposed analytical model, core material with a relative permeability $\mu_r = 10000$ is used first. Fig. 8 shows the currents in the healthy and short-circuited coils before and after one coil short-circuit. Here, the 3kW machine operates under rated condition and with $i_d = 0$ control.

In Fig. 8, the legend of the proposed analytical model in this paper is marked as "Proposed", the direct FE simulation results are labeled with "FE", and the results obtained using the analytical model proposed in [18] have also been added for the purpose of comparison. From Fig. 8, without considering the core saturation, a very good match (the errors between the currents of the analytical and FE models are less than 1%) can be observed between the results obtained by the proposed analytical (based on Matlab/Simulink) and FE models. However, if the influence of pole number and spatial distribution of coils on the determination of the inductances under fault is neglected like that in [18], the phase current and faulty coil current will be overestimated. In addition, the change in currents due to the one-coil short-circuit fault is also obvious. This is particularly the case for the current in the faulty coil, the peak value of which has increased from 4.24A to 38.6A. The change in phase currents and faulty coil current will also have an impact on the electromagnetic torque generated by the machine, as shown in Fig. 9.

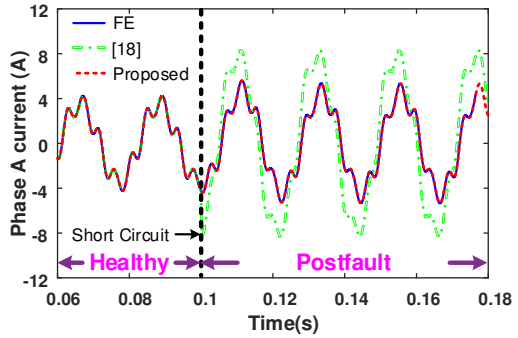

(a)

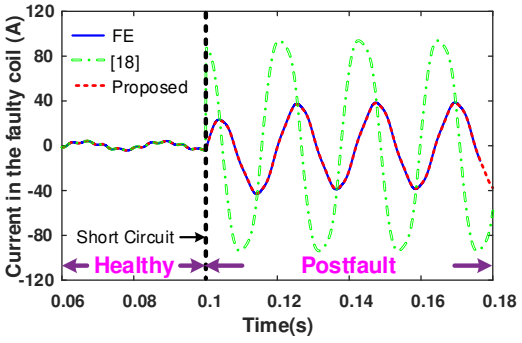

(b)

Fig. 8 Currents in (a) healthy coils and (b) short-circuited coil before and after one coil short-circuit.

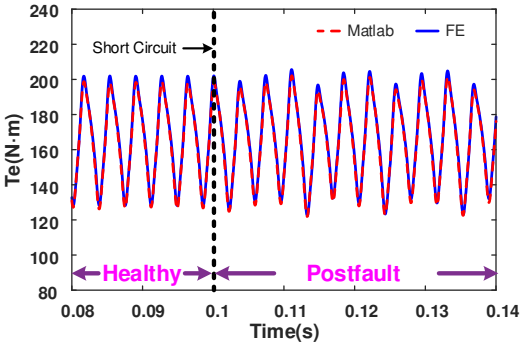

Fig. 9 Change of on-load torque of the 3kW SPM machine before and after the one coil short-circuit fault.

It is worth noting that the cogging torque obtained by the FE model has already been incorporated into the Simulink model to accurately capture the torque ripple characteristic before and

after the one coil short-circuit fault. It can be observed that although there is a slight discrepancy, both models predict a slight increase in torque ripple after the one-coil short-circuit fault.

To validate the accuracy of the proposed analytical model under different operating conditions, Fig. 10 shows the results of peak currents of phase A and short-circuited coil before and after the one coil short-circuit fault. As with the previous analysis, the q-axis current is maintained at a constant to produce the rated torque and only the rotor speed is changed. The good agreement in simulated results at different rotor speeds further confirms that the proposed analytical model is accurate.

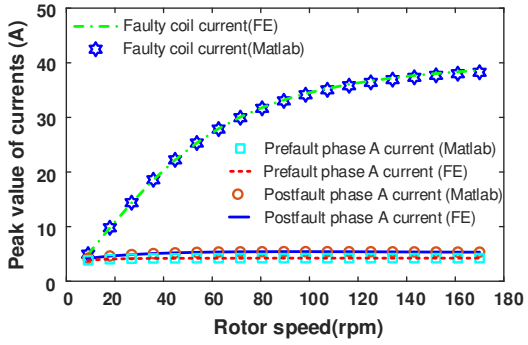

Fig. 10 Peak values of phase A currents of the 3kW SPM machine before and after one coil short-circuit fault.

b. *Nonlinear Magnetic Core Material*

If the core saturation is considered, there will be some discrepancy between the simulated results obtained by the proposed analytical (based on Matlab/Simulink) and the non-linear FE models, as shown in Fig. 11. In order to improve the model accuracy while considering the core saturation effect in the Simulink model, the proposed method in Fig. 3 has been employed. As can be seen from Fig. 11 that the error between the currents of the analytical and FE models is now reduced from 16% to 8%. It should be mentioned that only one iteration in Fig.3 is used to obtain the on-load PM flux linkages and saturated inductances in the Simulink model. This is why there is still an 8% difference between the analytical and FE fault currents. More iterations will reduce this difference further but will be more time consuming and add extra model complexity.

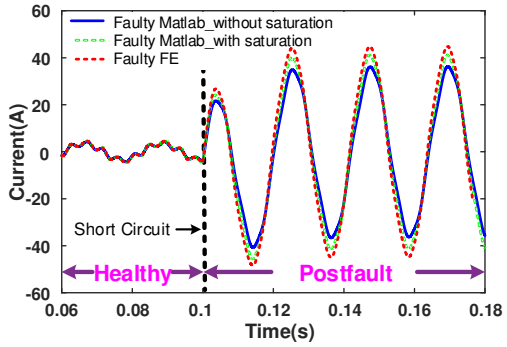

Fig. 11 Currents in phase A when the saturation is considered in the analytical and FE models.

B. *Single Turn Short-Circuit Fault*

Similar to the one coil short-circuit fault, the single turn short-circuit fault has also been investigated, and the results are shown in Fig. 12. A generally good agreement can be observed between the results obtained by the analytical (based on Matlab/Simulink) and FE models. It is noticed that under the single turn short-circuit fault, the faulty phase turn ratio is $\mu = 1/832$, which is too small to cause variations in current waveforms in the healthy windings. However, as expected, the single turn short-circuit leads to the highest short-circuit current (almost 27 times the rated current while for the one coil short circuit fault, it is about 10 times). This extremely large single turn short-circuit current could lead to serious local overheating problems. So it is still important to detect such faults in order to take measures to prevent further damage to the machine. However, this is out of scope of this paper and will be part of our future research.

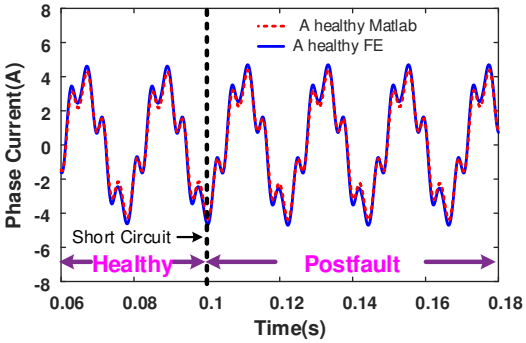

(a)

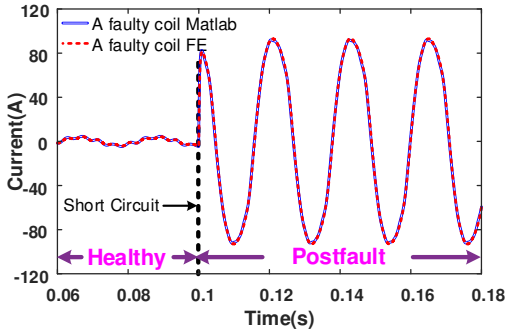

(b)

Fig. 12 Currents in (a) healthy coils and (b) short-circuited turn before and after one turn short-circuit fault.

The peak currents at different rotor speeds under single turn short-circuit fault have also been simulated, as shown in Fig. 13.

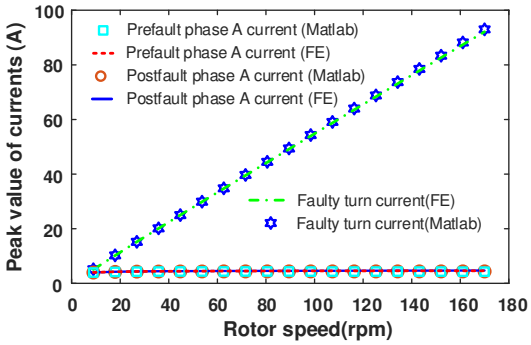

Fig. 13 Peak currents in phase A of the 3kW SPM machine before and after single turn short-circuit fault.

Interestingly, the single turn short circuit current seems to increase linearly with the rotor speed for the full investigated

speed range. This phenomenon can be explained by using the voltage equation of the short-circuited path to predict the amplitude of the short-circuited current. To simplify the analysis, it is assumed that after the ITSC fault, the motor currents are almost unchanged. If all harmonics in the phase currents and back EMFs are neglected, then the following equation to predict the amplitude of the short-circuited current for the 3kW SPM machine is valid

$$I_f \approx \frac{\mu\omega_r\lambda_m}{\sqrt{(\mu R_s)^2 + \left(\omega_r L_f\right)^2}} \tag{15}$$

where λ_m is the amplitude of the open-circuit phase flux linkage. When the rotor speed is low, the resistance in the denominator of (15) is much greater than the reactance, thus the amplitude of the short-circuited current increases linearly with the rotor speed. If the rotor speed goes higher and higher, the reactance will be the more important term in the denominator, and the amplitude of the short-circuited current will become almost constant, similar to what is shown in Fig. 10. It is estimated that the maximum short-circuit current for the one coil short-circuit fault is about 40.5A. However, the maximum single-turn short-circuit current is much higher, up to 1419.9A. If $\omega_r L_f = 1/3\mu R_s$ is used as the critical point for the "linear region" in the current-speed curves, then for the one-coil short-circuit fault, the critical rotor speed is about 23rpm, beyond which the increase rate of short-circuit current reduces. However, for the single turn short-circuit fault, the critical rotor speed for the "linear region" is around 803rpm. This means that the single-turn short-circuit current will increase linearly with rotor speed within a quite wide speed range.

C. Performance Comparison of Different Power Ratings

It is worth noting that the proposed analytical model is general for all PM machines with series-connected coils and can be used to investigate the fault performance of PM machines with different power ratings. A comparison in terms of fault tolerant capability amongst PM machines with different power ratings, e.g. 3kW, 0.5MW and 3MW has been carried out, and the results are shown in Fig. 14 and Fig. 15.

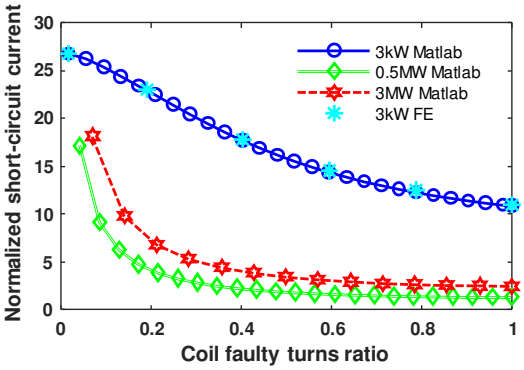

Fig. 14 Normalized short-circuit current versus coil faulty turns ratio.

In this comparative study, considering that the core saturation will not lead to a big difference in predictions of the short-circuited current, hence the linear model is used for simplicity. In Fig. 14 and Fig. 15, FE simulations of single turn, 10 turns, 21 turns, 31turns, 41 turns and one entire coil short-circuited faults for the 3kW machine have been carried out to compare against the analytical model based on Matlab/Simulink. However, the FE modelling for higher power ratings is significantly time consuming because large number of slots and poles exist and full models are needed when inter-turn short-circuits occur, and hence it has not been carried out in this paper. All data points in Fig. 14 and Fig. 15 are obtained when the machine operates under rated condition and with $i_d = 0$A control. It is apparent from Fig. 14 and Fig. 15 that large-power machines with series-connected coils are generally more fault-tolerant to the ITSC fault, but they are still vulnerable to short-circuit fault when a relatively small number of turns are short-circuited.

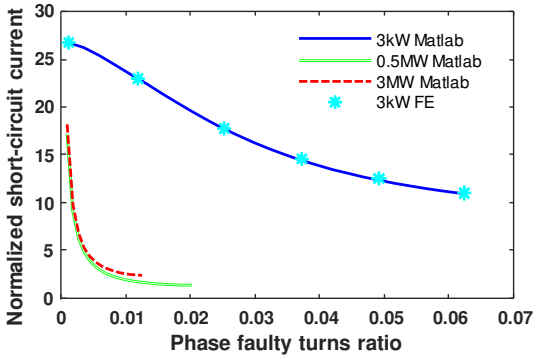

Fig. 15 Normalized short-circuit current versus phase faulty turns ratio.

V. Experimental Validation

A. Machine Prototype and Experimental Setup

A 12-slot 4-pole SPM machine prototype with internal rotor has been built and the ITSC faults are introduced to validate the proposed fault model. The main machine specifications are listed in Table III and the stator is shown in Fig. 16 (a). three fault scenarios can be introduced, i.e., single-turn, half-a-coil, and one-coil short-circuit faults. Because the main purpose of the experiments is to validate the proposed fault model, the SPM machine is used as a generator driven by a dc machine. In this way, no sophisticated control algorithm is needed, and the experimental setup can be simplified, as shown in Fig. 17. Because the validation of the fault model requires rotor speed as an input, the position encoder together with dSPACE in Fig. 17 are used to accurately capture the speed information (DC and ripple components).

Table III Specifications of 12-slot 4-pole SPM machine

Rated speed (rpm)	400	Stator outer diameter (mm)	100
Rated current rms (A)	2.5	Rotor outer diameter (mm)	49
Series turns/coil	40	Airgap length (mm)	1
Slots/poles	12/4	Stack length (mm)	50

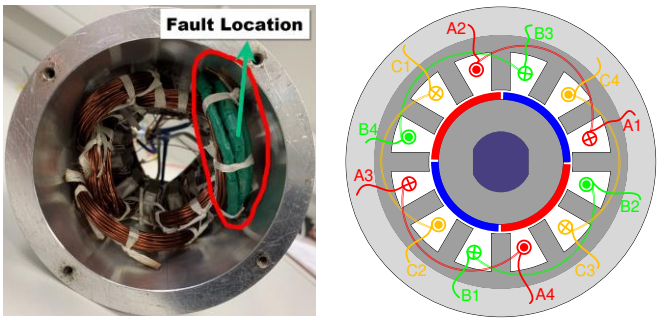

(a) (b)

Fig. 16 (a) Stator and (b) Winding layout of the 12-slot 4-pole SPM machine with ITSC fault.

The winding layout of this 12-slot 4-pole SPM machine is shown in Fig. 16 (b). All the coil ends (labelled as A1 to A4, B1 to B4 and C1 to C4) will be connected outside of the machine housing. On the other hand, the associated circuit schematic is illustrated in Fig. 18, in which each phase has two coils connected in series. The ITSC fault to be implemented occurs in A1A2 coil of the phase A. It is worth mentioning that no extra current limiting resistor is added to R_f in the short-circuited path. However, $R_f \neq 0$ because the resistive effect caused by the extension wires and the electrical contact have to be included, particularly when fewer turns are short-circuited. The value of R_f can be obtained by subtracting R_{Af} from $R_f + R_{Af}$. It should be mentioned that both R_{Af} and $R_f + R_{Af}$ can be measured by using a low resistance instrument like Rhopoint Milli-Ohmmeter M210 or Hioki IM3570 Impedance Analyzer before the ITSC is introduced. For the single-turn, half-a-coil, and one-coil short circuit faults, the measured values of R_f are 0.036Ω, 0.031Ω, and 0.033Ω, respectively. As for R_{Af}, they are 0.007Ω, 0.145Ω, and 0.323Ω, respectively.

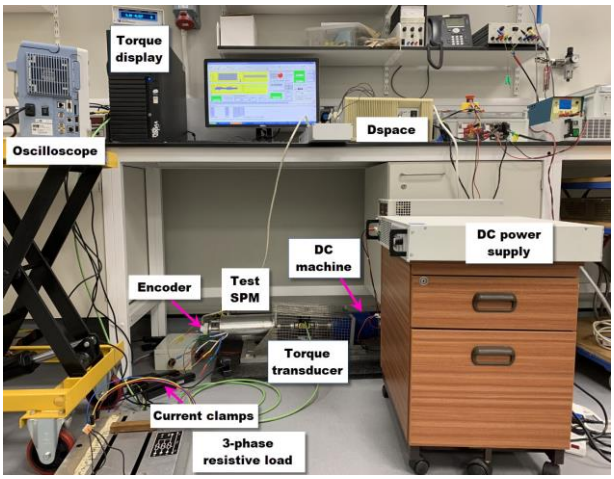

Fig. 17 Experimental setup.

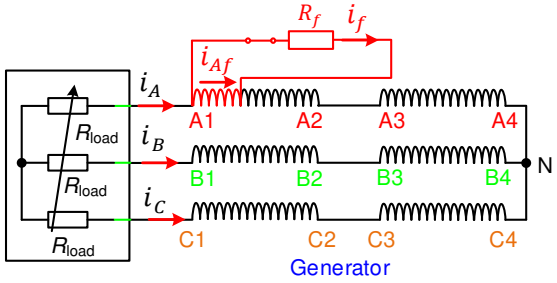

Fig. 18 Circuit schematic showing the introduced ITSC fault.

B. Cogging Torque and Back EMFs

As mentioned previously, the cogging torque needs be included in the analytical model built in Matlab/Simulink to predict the torque ripple more accurately. The cogging torque obtained from the 2D FE model and experimental measurement using the method in [29] is shown in Fig. 19. It is noticed that the cogging torque of the test machine is quite large relative to the torque output capability of the driving dc machine. At low speed, it could not be overcome by the developed torque of the dc machine, and thus it prevents the test motor from spinning. The cogging torque also acts as a torque disturbance to the dc machine to cause speed variations, especially at low speed, as will be investigated in section V.D.

On the other hand, to avoid the negative impact of relatively large speed variations on the back EMFs measurement, a rotor speed of 900rpm has been adopted for the simulated and measured back EMFs of A1A2 coil as shown in Fig. 20 (a). As mentioned earlier, the harmonics of the phase back EMFs, as shown in Fig. 20 (b), can be included into the proposed model to predict currents more accurately.

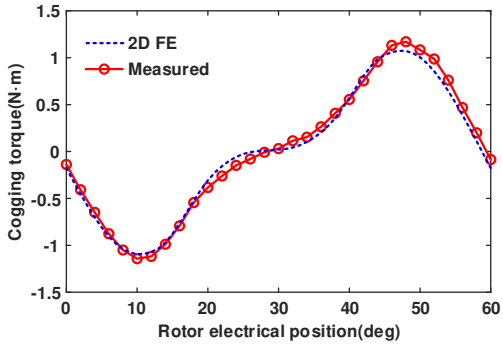

Fig. 19 Cogging torque obtained from the 2D FE model and measurement.

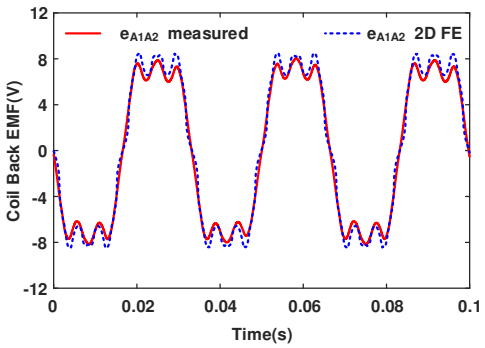

(a)

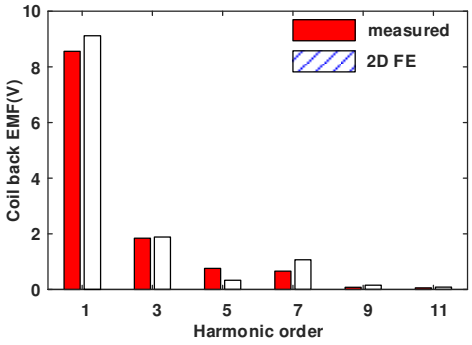

(b)

Fig. 20 Measured and 2D FE predicted back EMFs of A1A2 coil. (a) waveforms and (b) spectra.

C. 2D and 3D FE Inductances

The analytical method proposed in this paper to calculate the 2D linear FE inductances under ITSC faults is applied to this 12-slot 4-pole SPM machine. To simplify the calculation of the slot-leakage inductances, the trapezoidal slot shown in Fig. 16 (b) is approximated to a rectangular slot with equal height and area. With this approximation, the inductances have been calculated and results are shown in Table IV. It should be mentioned that all the FE inductances are average values over one electrical period. From Table IV, a generally good

agreement between the analytical and FE results can be observed.

In addition, the effect of core saturation on inductance values can also be observed based on the results in Table IV. It can be seen that when core saturation is considered, the inductance values drop significantly, therefore the core saturation cannot be neglected. It is also worth noting that as the length of end-winding at each side is almost equal to the stack length, the end-windings cannot be neglected during the inductance calculations either. To make a direct comparison against the measured inductances using Hioki IM3570 Impedance Analyzer, a 3D FE model has been built (see Fig. 21) and the 3D FE and measured inductances are shown in Table V.

Table IV Inductances in mH of the machine prototype under one coil short-circuit fault

Method	$L_{AA}/L_{BB}/L_{CC}$	$M_{AB}/M_{BC}/M_{AC}$	M_{Bf}/M_{Cf}	$M_{Ah,f}$
Analytical	1.148	-0.328	-0.164	-0.246
2D FE (Linear)	1.116	-0.3	-0.15	-0.223
Error (%)	2.9	9.3	9.3	10.3
2D FE (Nonlinear)	0.85	-0.21	-0.105	-0.08
Difference (%)	31.3	42.9	42.9	178.8

Note: the difference (%) in the last row is between the 2D FE (linear) and 2D FE (nonlinear)

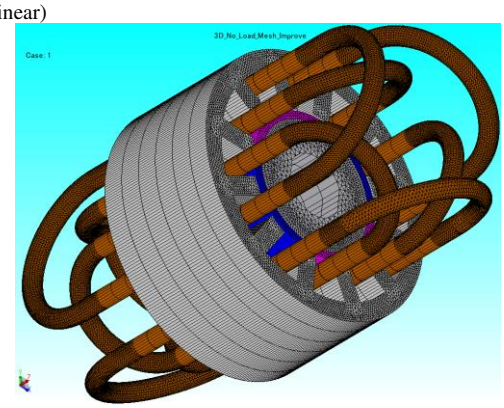

Fig. 21 3D FE model of the 12-slot 4-pole SPM machine.

Table V Phase self- and mutual-inductances in mH of the tested machine

Method	$L_{AA}/L_{BB}/L_{CC}$	$M_{AB}/M_{BC}/M_{AC}$
3D FE (Nonlinear)	1.323/1.321/1.319	-0.264/-0.266/-0.265
Measurement	1.418/1.419/1.461	-0.283/-0.294/-0.296
Error(%)	-6.7/-6.7/-9.7	-6.7/-9.5/-10.5

From Table V, it is found that the discrepancies between the measured and 3D FE phase self- and mutual-inductances are relatively small, both of them can therefore be used in the simulations of healthy and faulty machine performance in the following sections.

D. Phase and Faulty Currents under Different Fault Scenarios

In this section, although three fault cases have been investigated, only the currents of one-coil and single-turn short-circuit faults are shown due to space limitations.

a. One-Coil Short-Circuit Fault

When the one-coil short-circuit fault is introduced, a 3-phase resistive load (see Fig. 18) of $R_{load} = 5\Omega$ is used to limit the amplitude of the phase currents. The measured speed is obtained from the encoder, as shown in Fig. 22. This speed is used in the simulation to fully consider the impact of speed ripple on the predicted current waveforms. The measured and predicted phase currents and the fault current (i_{Af}) in the short-circuited coil are shown in Fig. 23.

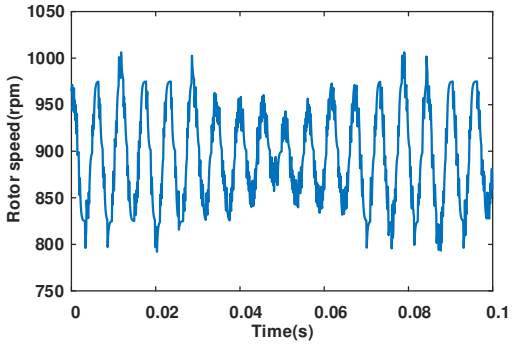

Fig. 22 Rotor speed under one-coil short-circuit fault.

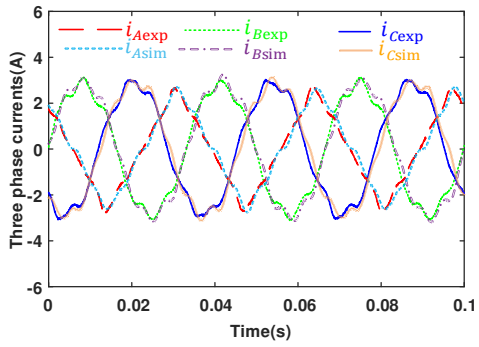

(a)

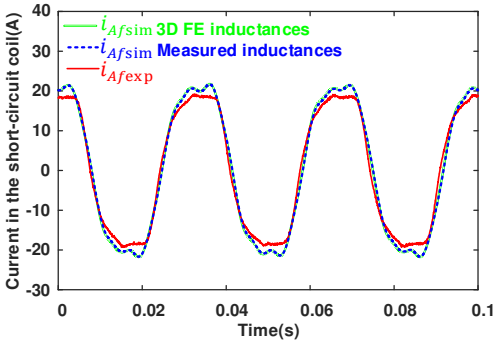

(b)

Fig. 23 (a) Phase currents and (b) fault current (i_{Af}) in the short-circuited coil under the one coil short-circuit fault.

In Fig. 23 (a), it is worth noting that, as the predicted phase currents obtained by using measured inductances and 3D FE inductances are very much the same, to make the comparison between the measured and predicted phase currents clearer, only the predicted phase currents using 3D FE inductances are shown. A generally good agreement can be observed between the predicted and measured phase currents. This is the same for the predicted and measured fault currents (i_{Af}) in the short-circuited coil, as shown in Fig. 23 (b), where the predicted fault currents (i_{Af}) both obtained by using 3D FE inductances and measured inductances have been presented.

b. *Single-Turn Short-Circuit Fault*

In this case, the 3-phase resistive load R_{load} (see Fig. 18) is also set to be 5Ω, and the tested motor starts under a single-turn short-circuit fault directly. The speed profile obtained from the encoder is similar to that shown in Fig. 22. The corresponding phase currents and current in the short-circuited turn are shown in Fig. 24. In Fig. 24(a), there is a very small difference between the predicted and measured phase currents. However, in Fig. 24(b), the difference between the fault current (i_{Af}) of the short-circuited path is relatively larger. This difference is mainly caused by the not very accurate measurement of single-turn resistance and by the neglected contact resistance between the connection points of the single turn when introducing the short-circuit fault. It is worth mentioning that the single turn resistance ($R_{Af} + R_f$) is only 43mΩ. Such a small value is very sensitive to any disturbance and it can be altered after introducing the short-circuit fault.

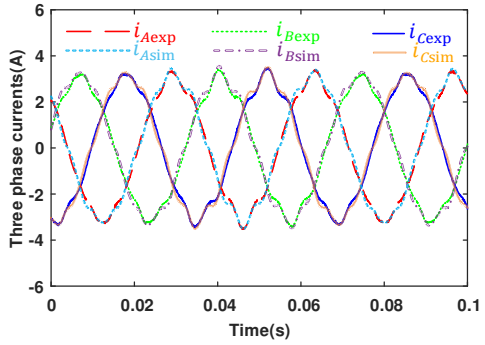

(a)

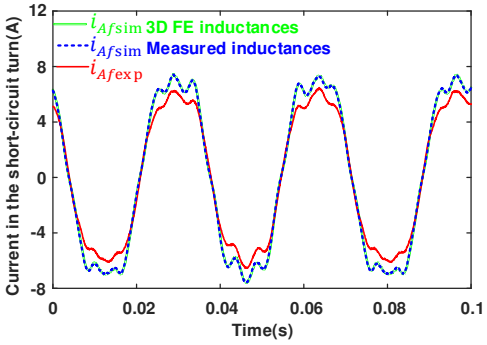

(b)

Fig. 24 (a) phase currents and (b) fault current (i_{Af}) in the short-circuited turn under the single turn short-circuit fault.

Compared with the one-coil short-circuit current in Fig. 23 (b), the single-turn short-circuit current shown in Fig. 24 (b) for this machine prototype is much lower, which is opposite to that observed for the 3kW one. This is mainly because for this 12-slot 4-pole machine, not a perfectly full single-turn short-circuit fault is introduced, i.e. $R_f = 0.036\Omega \neq 0\Omega$, which is about 5 times the resistance of short-circuited turns ($R_{Af} = 0.007\Omega$). In addition, for this tested machine operating at 900rpm, the resistances are at least 2.5 times the corresponding inductive impedances. As a result, the inductive impedance in (15) could be neglected for simplification. This allows for an estimate of the amplitude of the fundamental component of i_f by using

$$I_f \approx \frac{\mu\omega_r\lambda_m}{(R_f + R_{Af})} \tag{16}$$

For the one-coil short circuit fault, the estimated I_f is 25.6A. However, for the single-turn short circuit fault, I_f is only 5.23A. It is noticed that both estimated I_f are slightly higher than the corresponding measured results. This is due to slightly lower measured resistances, which cannot take the contact resistance into consideration when two terminals are connected to introduce the ITSC fault.

c. *Different Loads and Speeds*

Further validation of the proposed model has been carried out for different load conditions (different currents and rotor speeds). The currents (peak value) in the short-circuited coil A1A2 under two different resistive loads and different rotor speeds have been measured, as shown in Fig. 25. Again, the measured results generally match well with the simulated ones using the measured inductances, further proving the accuracy of the proposed fault model under various operating conditions.

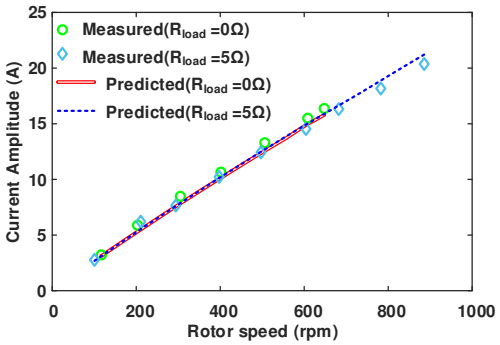

Fig. 25 Amplitude of current of the short-circuited coil under different resistive loads and speeds.

VI. Conclusion

This paper presents a general analytical model for fault performance evaluation of multipole PM wind power generators with different power ratings under inter-turn short-circuit (ITSC) fault. Simulation results from 2D FE and Simulink models match quite well when a linear magnetic material is used, which verifies the accuracy of the proposed analytical model. It is found that the influence of pole number and spatial distribution of coils on determination of inductances under fault cannot be neglected when the number of short-circuited turns in one coil is large. It is also found that the developed analytical model could be used to obtain current profiles, which can be used as inputs in the nonlinear FE fault model to obtain the saturated inductances and on-load PM flux linkages in order to improve the prediction of fault performance under core saturation. As for fault-tolerant capability, large power machines with all coils connected in series are generally much more fault-tolerant to ITSC fault. However, they are still vulnerable to faults when relatively small number of turns are short-circuited. Finally, the proposed fault model is validated by a series of experiments on a 12-slot 4-pole machine prototype.

REFERENCES

[1] N. M. A. Freire and J. Marques Cardoso Antonio, "Fault detection and condition monitoring of PMSGs in offshore wind turbines," *Machines*, vol. 9, no. 11, p. 260, 2021.

[2] B. Lu, Y. Li, X. Wu, and Z. Yang, "A review of recent advances in wind turbine condition monitoring and fault diagnosis," in *2009 IEEE Power Electronics and Machines in Wind Applications*, Jun. 2009, pp. 1–7.

[3] F. Blaabjerg, M. Liserre, and K. Ma, "Power electronics converters for wind turbine systems," *IEEE Trans. Ind. Appl.*, vol. 48, no. 2, pp. 708–719, Mar. 2012.

[4] K. Alewine and W. Chen, "A review of electrical winding failures in wind turbine generators," *IEEE Elect. Insul. Mag.*, vol. 28, no. 4, pp. 8–13, Jul. 2012.

[5] A. H. Bonnett and G. C. Soukup, "Cause and analysis of stator and rotor failures in three-phase squirrel-cage induction motors," *IEEE Trans. Ind. Appl.*, vol. 28, no. 4, pp. 921–937, Jul. 1992.

[6] X. Tu, L. Dessaint, N. Fallati, and B. D. Kelper, "Modeling and real-time simulation of internal faults in synchronous generators with parallel-connected windings," *IEEE Trans. Ind. Electron.*, vol. 54, no. 3, pp. 1400–1409, Jun. 2007.

[7] T. Kim, H. Lee, and S. Kwak, "The internal fault analysis of brushless DC motors based on the winding function theory," *IEEE Trans. Magn.*, vol. 45, no. 5, pp. 2090–2096, May 2009.

[8] K. Kim, J. Park, J. Hur, and B. Kim, "Comparison of the fault characteristics of IPM-type and SPM-type BLDC motors under inter-turn fault conditions using winding function theory," *IEEE Trans. Ind. Appl.*, vol. 50, no. 2, pp. 986–994, Mar. 2014.

[9] M. Ojaghi and V. Bahari, "Rotor damping effects in dynamic modeling of three-phase synchronous machines under the stator interturn faults—winding function approach," *IEEE Trans. Ind. Appl.*, vol. 53, no. 3, pp. 3020–3028, May 2017.

[10] Z. T. Mei, G. J. Li, Z. Q. Zhu, R. Clark, A. Thomas, and Z. Azar, "Scaling effect on inter-turn short-circuit of PM machines for wind power application," in *2021 IEEE International Electric Machines and Drives Conference (IEMDC)*, 2021, pp. 1–8.

[11] B. Ge, S. Xiao, Z. Liu, D. Tao, and X. Sun, "Improved model of synchronous generators internal faults based on circuit-coupled FEM," *IEEE Trans. Energy Convers.*, vol. 32, no. 3, pp. 876–884, Sep. 2017.

[12] M. Zafarani, E. Bostanci, Y. Qi, T. Goktas, and B. Akin, "Interturn short-circuit faults in permanent magnet synchronous machines: an extended review and comprehensive analysis," *IEEE J. Emerg. Sel. Top. Power Electron.*, vol. 6, no. 4, pp. 2173–2191, Dec. 2018.

[13] A. Berzoy, A. A. S. Mohamed, and O. Mohammed, "Impact of inter-turn short-circuit location on induction machines parameters through FE computations," *IEEE Trans. Magn.*, vol. 53, no. 6, pp. 1–4, Jun. 2017.

[14] P. Naderi, "Magnetic-equivalent-circuit approach for inter-turn and demagnetisation faults analysis in surface mounted permanent-magnet synchronous machines using pole specific search-coil technique," *IET Electr. Power Appl.* , vol. 12, no. 7, pp. 916–928, 2018.

[15] G. Forstner, A. Kugi, and W. Kemmetmüller, "A magnetic equivalent circuit based modeling framework for electric motors applied to a PMSM with winding short circuit," *IEEE Trans. Power Electron.*, vol. 35, no. 11, pp. 12285–12295, 2020.

[16] P. Krause, O. Wasynczuk, and S. D. Sudhoff, *Analysis of Electric Machinery and Drive Systems*, 2nd ed. Wiley, 2002.

[17] H. A. Toliyat and T. A. Lipo, "Transient analysis of cage induction machines under stator, rotor bar and end ring faults," *IEEE Trans. Energy Convers.*, vol. 10, no. 2, pp. 241–247, Jun. 1995.

[18] L. Romeral, J. C. Urresty, J. R. Ruiz, and A. G. Espinosa, "Modeling of surface-mounted permanent magnet synchronous motors with stator winding interturn faults," *IEEE Trans. Ind. Electron.*, vol. 58, no. 5, pp. 1576–1585, May 2011.

[19] L. S. Maraaba, Z. M. Al-Hamouz, and M. A. Abido, "Mathematical modeling, simulation and experimental testing of interior-mount LSPMSM under stator inter-turn fault," *IEEE Trans. Energy Convers.*, vol. 34, no. 3, pp. 1213–1222, Sep. 2019.

[20] D. S. B. Fonseca, C. M. C. Santos, and A. J. M. Cardoso, "Stator faults modeling and diagnostics of line-start permanent magnet synchronous motors," *IEEE Trans. Ind. Appl.*, vol. 56, no. 3, pp. 2590–2599, 2020.

[21] B. Sen, J. Wang, and P. Lazari, "A high-fidelity computationally efficient transient model of interior permanent-magnet machine with stator turn fault," *IEEE Trans. Ind. Electron.*, vol. 63, no. 2, pp. 773–783, Feb. 2016.

[22] A. Sarikhani and O. A. Mohammed, "Inter-turn fault modeling of a variable speed PM wind generator using physics-based approach," in *2011 IEEE International Electric Machines Drives Conference (IEMDC)*, May 2011, pp. 636–641.

[23] T. W. Nehl, F. A. Fouad, and N. A. Demerdash, "Determination of saturated values of rotating machinery incremental and apparent inductances by an energy perturbation method," *IEEE Trans. Power App. Syst.**, vol. PAS-101, no. 12, pp. 4441–4451, Dec. 1982.

[24] J. K. Tangudu, T. M. Jahns, A. M. El-Refaie, and Z. Q. Zhu, "Segregation of torque components in fractional-slot concentrated-winding interior PM machines using frozen permeability," in *2009 IEEE Energy Conversion Congress and Exposition*, Sep. 2009, pp. 3814–3821.

[25] B. Vaseghi, B. Nahid-mobarakh, N. Takorabet, and F. Meibody-Tabar, "Inductance identification and study of PM motor with winding turn short circuit fault," *IEEE Trans. Magn.*, vol. 47, no. 5, pp. 978–981, May 2011.

[26] J. R. Hendershot and T. J. E. Miller, *Design of Brushless Permanent-Magnet Machines*. Motor Design Books, 2010.

[27] T. A. Lipo, *Analysis of Synchronous Machines*, 2nd ed. CRC Press, 2012.

[28] Z. Sun, J. Wang, D. Howe, and G. Jewell, "Analytical prediction of the short-circuit current in fault-tolerant permanent-magnet machines," *IEEE Trans. Ind. Electron.*, vol. 55, no. 12, pp. 4210–4217, Dec. 2008.

[29] Z. Q. Zhu, "A simple method for measuring cogging torque in permanent magnet machines," in *2009 IEEE Power Energy Society General Meeting*, 2009, pp. 1–4.